Out-of-Plane Ferroelectricity in Two-Dimensional 1T‴-MoS₂ Above Room Temperature

Changan HuangFu, Yaming Zhou,* Changming Ke, Junyi Liao, Jiangcai Wang, Huan Liu, Dameng Liu, Shi Liu,* Liming Xie,* and Liying Jiao*

Read Online

ABSTRACT: Two-dimensional (2D) molybdenum disulfide (MoS₂), one of the most extensively studied van der Waals (vdW) materials, is a significant candidate for electronic materials in the post-Moore era. MoS₂ exhibits various phases, among which the 1T‴ phase possesses noncentrosymmetry. 1T‴-MoS₂ was theoretically predicted to be ferroelectric a decade ago, but this has not been experimentally confirmed until now. Here, we have prepared high-purity 2D 1T‴-MoS₂ crystals and experimentally confirmed the room-temperature out-of-plane ferroelectricity. The noncentrosymmetric crystal structure in 2D 1T‴-MoS₂ was convinced by atomically resolved transmission electron microscopic imaging and second harmonic generation (SHG) measurements. Further, the ferroelectric polarization states in 2D 1T‴-MoS₂ can be switched using piezoresponse force microscopy (PFM) and electrical gating in field-effect transistors (FETs). The ferroelectric-to-paraelectric transition temperature is measured to be about 350 K. Theoretical calculations have revealed that the ferroelectricity of 2D 1T‴-MoS₂ originates from the intralayer charge transfer of S atoms within the layer. The discovery of intrinsic ferroelectricity in the 1T‴ phase of MoS₂ further enriches the properties of this important vdW material, providing more possibilities for its application in the field of next-generation electronic devices.

KEYWORDS: two-dimensional, out-of-plane, ferroelectricity, MoS₂, phase engineering
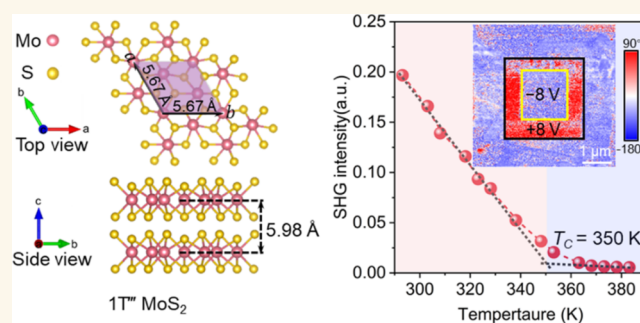
INTRODUCTION

Two-dimensional (2D) van der Waals (vdW) ferroelectrics, atomically thick materials with electrically switchable spontaneous polarization, have recently emerged as promising elements for the post-Moore's era electronics. 2D vdW ferroelectrics offer key material bases for the development of various innovative nanoelectronics devices, such as high-density capacitors,[1] beyond-Boltzmann transistors,[2] nonvolatile memory,[3] and so on.[4] The noncentrosymmetric atomic structure is a prerequisite for ferroelectricity. To date, very limited 2D vdW intrinsic ferroelectrics have been reported, such as $CuInP_2S_6$,[5] In_2Se_3,[6] WTe_2,[7] $MoTe_2$,[8] Bi_2O_2Se,[9] and so on. Therefore, the continuous exploration of more 2D intrinsic ferroelectrics is essential. 2D MoS₂ has polymorph structures, such as semiconducting 2H phase and metallic 1T and 1T′ phases. Recently, the polarization reversal of 1T″-MoS₂ has been achieved via mechanical pressure provided by a scanning probe microscope tip based on the flexoelectric effect.[10] In 2014, Shirodkar et al. predicted that a distorted 1T MoS₂

structure with a $\sqrt{3}a \times \sqrt{3}a$ supercell (also named as 1T‴ phase MoS₂[11]) can exhibit robust out-of-plane ferroelectricity,[12] and its calculated polarization value (0.18 $\mu C \cdot cm^{-2}$) is significantly higher than that (0.04 $\mu C \cdot cm^{-2}$) of 1T″-MoS₂. However, until now, theoretical predictions of the ferroelectricity of 1T‴-MoS₂ have not been verified experimentally.

Here, we report the synthesis of high-phase purity metastable 1T‴-MoS₂ and the experimental observation of room-temperature ferroelectricity. The synthesis of 1T‴-MoS₂ crystals was done via a two-step reduction−oxidation process with K_2MoS_4 as the starting material. Both atomically resolved microscopic imaging and second harmonic generation (SHG)
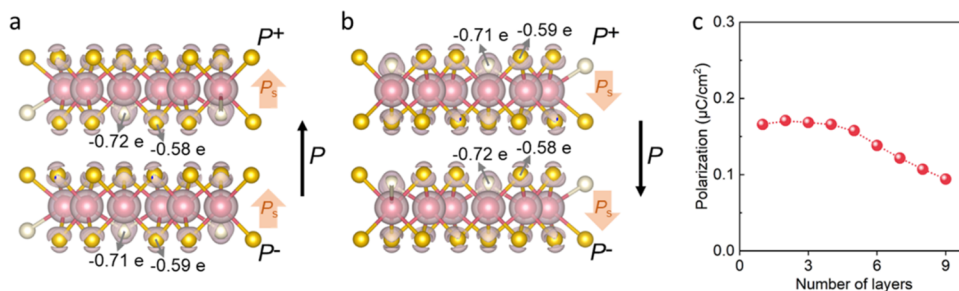
Figure 1. DFT calculations on the polarization in 2D 1T‴-MoS$_2$. (a, b) Charge density for the upward and downward polarizations in a bilayer 1T‴-MoS$_2$. (c) The dependence of polarization values on the number of layers in 2D 1T‴-MoS$_2$.
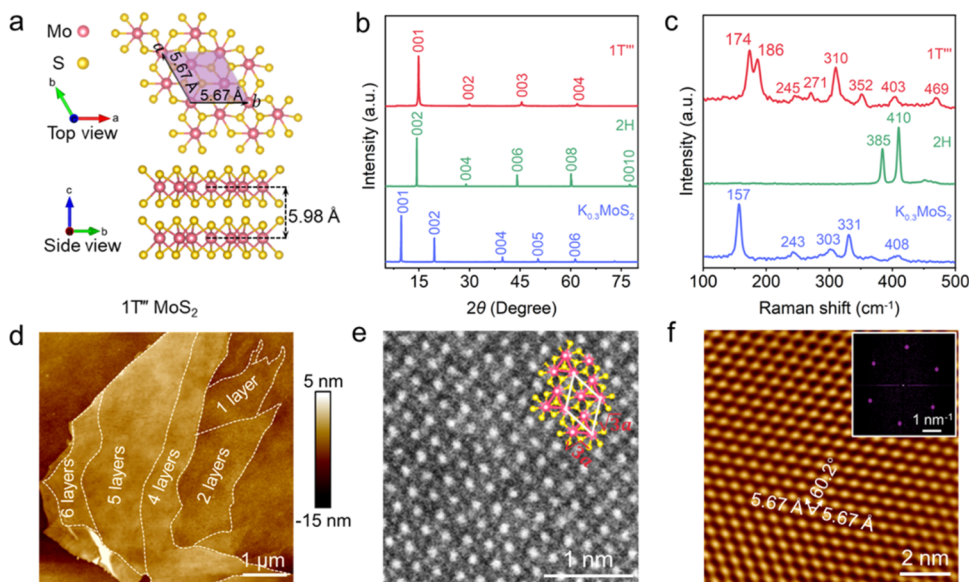

Figure 2. Structural characterizations of 1T‴-MoS$_2$. (a) Schematic top and side views of the 1T‴-MoS$_2$ structure. The pink and golden spheres represent the Mo atoms and S atoms, respectively. The purple rhombus shadow represents a primitive cell in the top view. (b) XRD patterns and (c) Raman spectra of 1T‴, 2H, and K$_{0.3}$MoS$_2$ crystals. (d) Atomic force microscopic (AFM) image of 1T‴-MoS$_2$ flakes with varying layer numbers obtained by gold-assisted exfoliation. (e) Scanning transmission electron microscopic (STEM) image of a 1T‴-MoS$_2$ flake. The pink and golden balls refer to the Mo atoms and S atoms, respectively. (f) LFM lattice image of a 1T‴-MoS$_2$ flake. Inset, the 2D fast Fourier transform (FFT) pattern of this image.

measurements confirmed the noncentrosymmetric superlattice in the mechanically exfoliated 2D 1T‴-MoS$_2$. The ferroelectric polarization could be switched by an external electric field in piezoresponse force microscopy (PFM). We further demonstrated that the polarization of 1T‴-MoS$_2$ can be toggled by gate voltage in field-effect transistor (FET) devices, as evidenced by the bistate switchable conductivities of both the material itself and the graphene electric field sensor, thereby validating the ferroelectricity in 1T‴-MoS$_2$.

RESULTS AND DISCUSSION

We conducted density functional theory (DFT) calculations on the thickness-dependent ferroelectricity in 1T‴-MoS$_2$ (see Experimental Section for details) since previous calculations have only been done on the monolayer 1T‴-MoS$_2$.[13] Our findings revealed that the intrinsic ferroelectricity in monolayer 1T‴-MoS$_2$ originates from the intralayer charge transfer of S atoms, leading to an out-of-plane polarization vector (Figure S1). For the bilayer, 1T‴-MoS$_2$ with the most energetically favorable A–A stacking (Figure S2a), its polarization naturally retained an overall upward or downward direction (Figures 1a,b and S2b). This polarization tended to remain constant for

up to four layers (Figure 1c). For five layers and more, a gradual decrease of polarization was observed (Figure 1c) due to the fact that the more electrons transferred can trigger the increase and shielding of depolarization potential (Figure S3). Nevertheless, the polarization persists in 1T‴-MoS$_2$ up to nine layers, the maximum number of layers we have examined (Figure 1c).

The relatively high formation energy of 1T‴-MoS$_2$ (220 meV higher than the 2H phase and 40 meV higher than the 1T′ phase[14]) poses difficulty in the synthesis of the crystal with high phase purity. A two-step reduction−oxidation process using K$_2$MoS$_4$ as a single precursor was utilized to synthesize 1T‴-MoS$_2$ bulk crystals. Initially, K$_2$MoS$_4$ powders were reduced by H$_2$ at 770 °C to produce high-purity K$_x$MoS$_2$ crystals (eq 1). Subsequently, the K$_x$MoS$_2$ crystals were treated with an acidified aqueous solution of K$_2$Cr$_2$O$_7$ to yield high-purity 1T‴-MoS$_2$ crystals (eq 2).

$$2K_2MoS_4 + 3H_2 \rightarrow 2K_xMoS_2 + (2-2x)K + K_2S$$
$$+ 3H_2S\uparrow \tag{1}$$
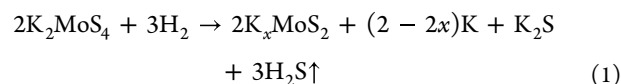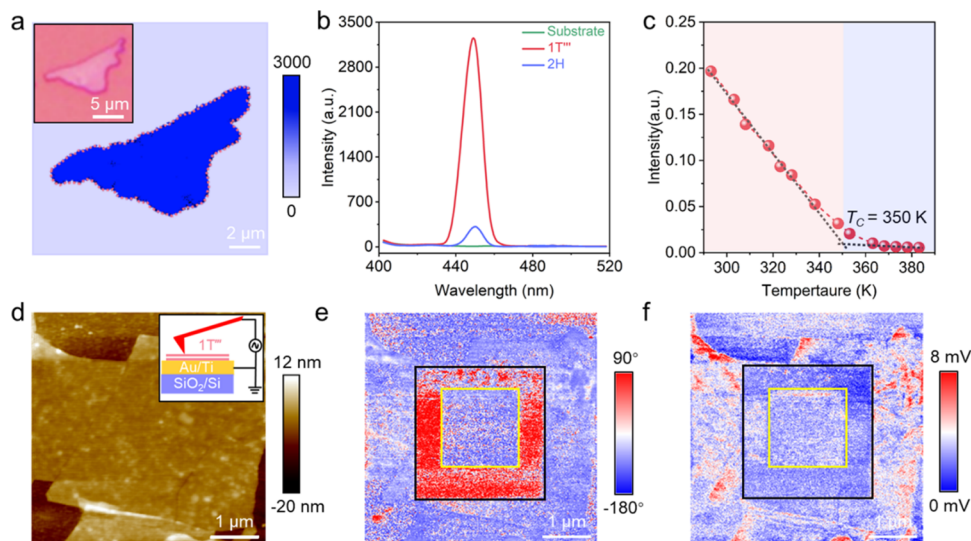
Figure 3. Broken symmetry and ferroelectric domain switch on 2D 1T‴-MoS$_2$ flakes. (a) SHG intensity mapping image of a 1T‴-MoS$_2$ flake. Inset: Corresponding optical image. (b) SHG spectra collected on the same flake of (a) before and after thermal annealing. (c) Temperature dependence of the SHG intensity of a 1T‴-MoS$_2$ flake (∼9.0 nm thick). (d) AFM topography of a 1T‴-MoS$_2$ flake before electrical poling by direct current (DC) bias. Inset: Schematics for the PFM testing setup. (e, f) Out-of-plane phase and amplitude images of the 1T‴-MoS$_2$ flake shown in (d) after electrical poling, where the black and yellow linear square patterns were written at +8 and −8 V, respectively.

$$6K_xMoS_2 + xCr_2O_7^{2-} + 14xH^+$$

$$\rightarrow 6MoS_2(1T''') + 6xK^+ + 7xH_2O + 2xCr^{3+} \quad (2)$$
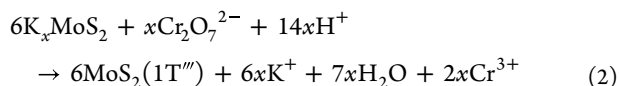
Various characterizations have been done on the obtained 1T‴-MoS$_2$ crystals. The energy-dispersive X-ray spectroscopy (EDS) measurements (Figure S4) revealed that the x value in K$_x$MoS$_2$ crystals acquired by eq 1 was ∼0.3. EDS also confirmed that no residual K ion existed in the 1T‴ samples obtained after the deintercalation of K ions from the K$_{0.3}$MoS$_2$ crystals as per eq 2. X-ray diffraction (XRD) confirmed that the crystal structures of the 1T‴ phase (trigonal $P3_1m$, Figure 2a) significantly differ from K$_{0.3}$MoS$_2$ crystals (monoclinic $C2/m$) and 2H phase (hexagonal $P6_3/mmc$)[15] (Figure 2b). The eight Raman characteristic peaks at 174 cm^{-1}, 186 cm^{-1} (J_1), 245 cm^{-1}, 271 cm^{-1} (J_3), 310 cm^{-1} (E_{1g}), 352 cm^{-1}, 403 cm^{-1} (A_{1g}), and 469 cm^{-1} arose from the obtained crystals were attributed to 1T‴-MoS$_2$,[16] which was completely different from the peaks of K$_{0.3}$MoS$_2$ and 2H crystals[17] (Figure 2c). Moreover, X-ray photoelectron spectroscopy (XPS) results further confirmed that 1T‴-MoS$_2$ crystals with high phase purity were synthesized through the moderate oxidation of K$_{0.3}$MoS$_2$ as per eq 2 (Figure S5). These combined characterizations led us to conclude that we have successfully prepared pure 1T‴-MoS$_2$ crystals.

To further determine the atomically resolved structure of 1T‴-MoS$_2$, we exfoliated 2D flakes with varied thickness onto Au/Ti-coated silicon substrates (Figure 2d) and then transferred the flakes to grids for high-angle annular dark-field (HAADF)-STEM imaging. HAADF-STEM images clearly revealed the trigonal trimerization of Mo atoms with a Mo−Mo distance of 3.01 Å (Figure 2e). This $\sqrt{3}a \times \sqrt{3}a$ superlattice structure is a characteristic feature of the 1T‴ phase, which is distinctly different from $\sqrt{3}a \times a$ for the 1T′ phase and $a \times a$ for the 2H phase (Figure S6). Lateral force microscopic (LFM) imaging revealed lattice constants of $a = b$ = 5.67 Å for 1T‴-MoS$_2$, matching well with the $\sqrt{3}a \times \sqrt{3}a$ superstructures (Figure 2f). These microscopic images confirm that the structure of the 2D 1T‴-MoS$_2$ we prepared precisely

matches the structures used in our theoretical calculations (Figures 1 and S1, S2).

2D 1T‴-MoS$_2$ we prepared can generate strong SHG signals due to the noncentrosymmetric structure (Figure S7), which is consistent with the results reported in previous studies.[16] Besides, the SHG mapping of the 1T‴-MoS$_2$ flake (Figures 3a and S8a) showed good uniformity, suggesting a high quality of the flake. After annealing at 260 °C, it converted the 1T‴ phase to the 2H phase (Figure S8b,c), and the SHG intensity of the annealed sample was reduced to 10% (Figure 3b), indicating that the pronounced second-order nonlinear optical properties of 1T‴-MoS$_2$ were inherent to its crystal structure. With the increase of the number of layers for 1T‴-MoS$_2$, the SHG intensity also increased, evidencing a noncentrosymmetric structure that was independent of layer numbers (Figure S8d). These SHG measurements indicate that our 1T‴-MoS$_2$ sample has a structure with spatial inversion symmetry breaking, which is indicative of potential ferroelectric polarization.

PFM electrical writing and polarization imaging were conducted on 2D 1T‴-MoS$_2$ flakes exfoliated on Au/Ti (5/5 nm)-covered Si substrates (Figure S9). A positive/negative DC bias between the conductive PFM tip and the substrate was used to switch the ferroelectric polarization, followed by application of an AC bias of 1 V to probe the ferroelectric domain (inset of Figure 3d). During the electrical writing, the morphology of the 1T‴-MoS$_2$ flake did not change (Figures 3d and S10a). The out-of-plane phase and amplitude displayed the distinct contrast between the two domains after writing a square-in-square pattern using opposing biases (±8 V) (Figure 3e,f). The written domain patterns remained stable after 12 h under ambient conditions (Figure S10b−d), ruling out potential influences from interface electrostatic or electrochemical phenomena.[18] The local PFM amplitude and phase hysteretic loops indicated a typical ferroelectric butterfly-like amplitude loop and a distinct 180° phase switching (Figure S10e), which further confirms the out-of-plane ferroelectricity in the 1T‴-MoS$_2$ flakes. In addition, polarization domain
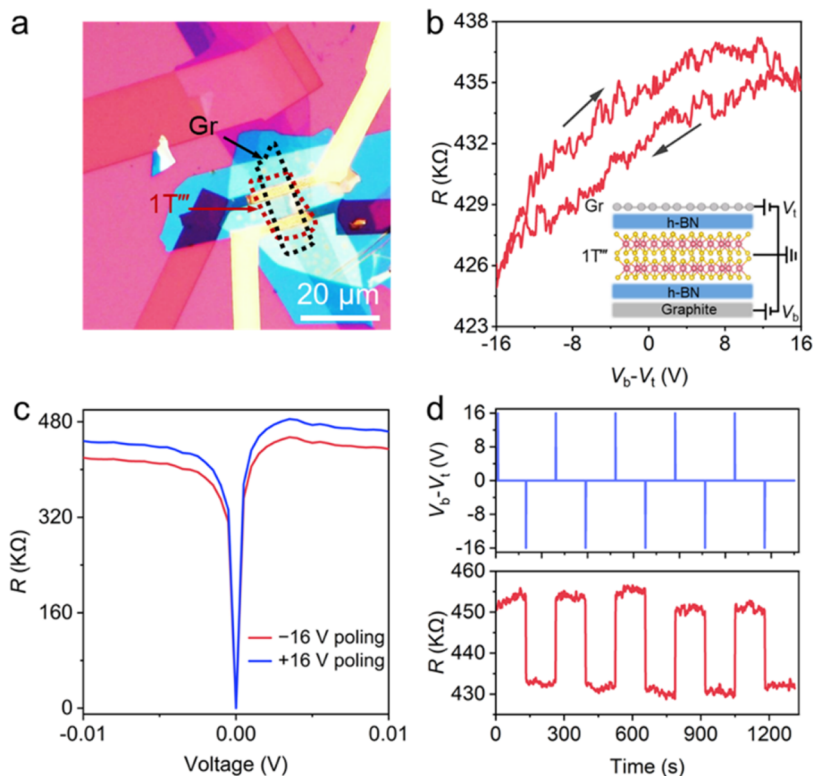
Figure 4. Switching characteristics of 2D 1T'''-MoS$_2$ in a FET device. (a) Optical image of the FET device. (b) Resistance of a typical 2D 1T'''-MoS$_2$ ($\sim$6.0 nm thick) as a function of $V_b - V_t$ in both forward and backward scan directions at T = 300 K. The arrows represent the direction of the hysteresis. Inset, the cross-sectional schematic used to apply a perpendicular electric field to the 2D 1T'''-MoS$_2$ channel. (c) $R-V$ curves of the 2D 1T'''-MoS$_2$ following the application of $V_b - V_t = \pm16$ V polarization. (d) Switch of the resistance state of 1T'''-MoS$_2$ by the alternative application of $V_b - V_t = \pm16$ V polarization at T = 300 K. The 1T'''-MoS$_2$ in the above devices was measured at a bias voltage of 10 mV.

inversion could also be visualized in other thinner 1T'''-MoS$_2$ samples (Figure S11). The value of the switching field decreased with increasing flakes thickness (Figure S12). These observations therefore show that the polarization of 1T'''-MoS$_2$ can be altered in response to an external bias.

We further investigated the ferroelectricity of 2D 1T'''-MoS$_2$ by incorporating a 1T'''-MoS$_2$ flake into two types of FET devices. In these devices, we manipulated the polarization direction of the flake by applying a gate voltage, which, in turn, induced changes in its own conductivity or that of the adjacent graphene layer, depending on the device configurations. The first type of FET device used 1T'''-MoS$_2$ flake as a channel, sandwiched in the vertically stacked van der Waals heterostructure of graphene/BN/1T'''-MoS$_2$/BN/graphite (Figures 4a and S13), in which graphene and graphite as the top and bottom gate electrodes, respectively. 1T'''-MoS$_2$ exhibited semiconducting characteristics in resistance–temperature ($R-T$) measurements (Figure S14a), but a very weak gate-dependent conductivity was observed (Figure S14b,c), which might be due to the ultrasmall band gap of 1T'''-MoS$_2$ (70 meV for $\sim$6 nm thick sample) (Figure S3d). The resistance of 1T'''-MoS$_2$ was measured at different vertical electrical fields applied through the top and bottom gate electrodes. A clockwise resistance hysteresis loop was observed (Figure 4b), which is a significant indication of out-of-plane ferroelectricity. Reversible polarization switching was tested by applying an alternative gate voltage at $V_b - V_t = \pm16$ V. The measured resistances showed two different values of 463.6 kΩ (after +16 V poling) and 434.4 kΩ (after −16 V poling)

(Figure 4c,d). The two resistance states could maintain over 2000 s (Figure S15). After annealing the device at 260 °C (Figure S16a), the resistance switching disappeared (Figure S16b,c) because 1T'''-MoS$_2$ was converted to 2H-MoS$_2$, which is not ferroelectric.[19] Besides, temperature-dependent SHG measurements were done on the 2D 1T'''-MoS$_2$, in which the SHG intensity of 1T'''-MoS$_2$ flake gradually decreased with the increase of temperature and vanished above 370 K (Figure 3c). The ferroelectric-to-paraelectric phase transition temperature (T_C) of 1T'''-MoS$_2$ was measured to be $\sim$350 K, which is below the phase structure transition temperature (393 K) of the 1T''' phase to the 2H phase (Figure S17) and higher than T_C of several previously reported 2D ferroelectric materials, such as CuInP$_2$S$_6$,[20] MoTe$_2$,[8] and WTe$_2$.[21]

The measurements conducted using the first device geometry have confirmed that the intrinsic 1T'''-MoS$_2$ can be polarized. However, the difference between the two resistance states produced by polarization is relatively small, which may be related to its small band gap. Therefore, we adopted another device geometry, which has been successfully used to detect the ferroelectricity of 2D metallic materials by using monolayer graphene as a sensing channel.[7] This device was composed of four layers of vertically stacked 2D vdW materials sandwiched between two electrodes. A single-layered graphene served as the channel material (insets of Figures 5a and S18a), connected to the source and drain electrodes. Its conductance can be tuned by both the graphite bottom gate voltage (V_b) and the 1T'''-MoS$_2$ top gate voltage (V_t). This configuration allows for independent control of the carrier density in
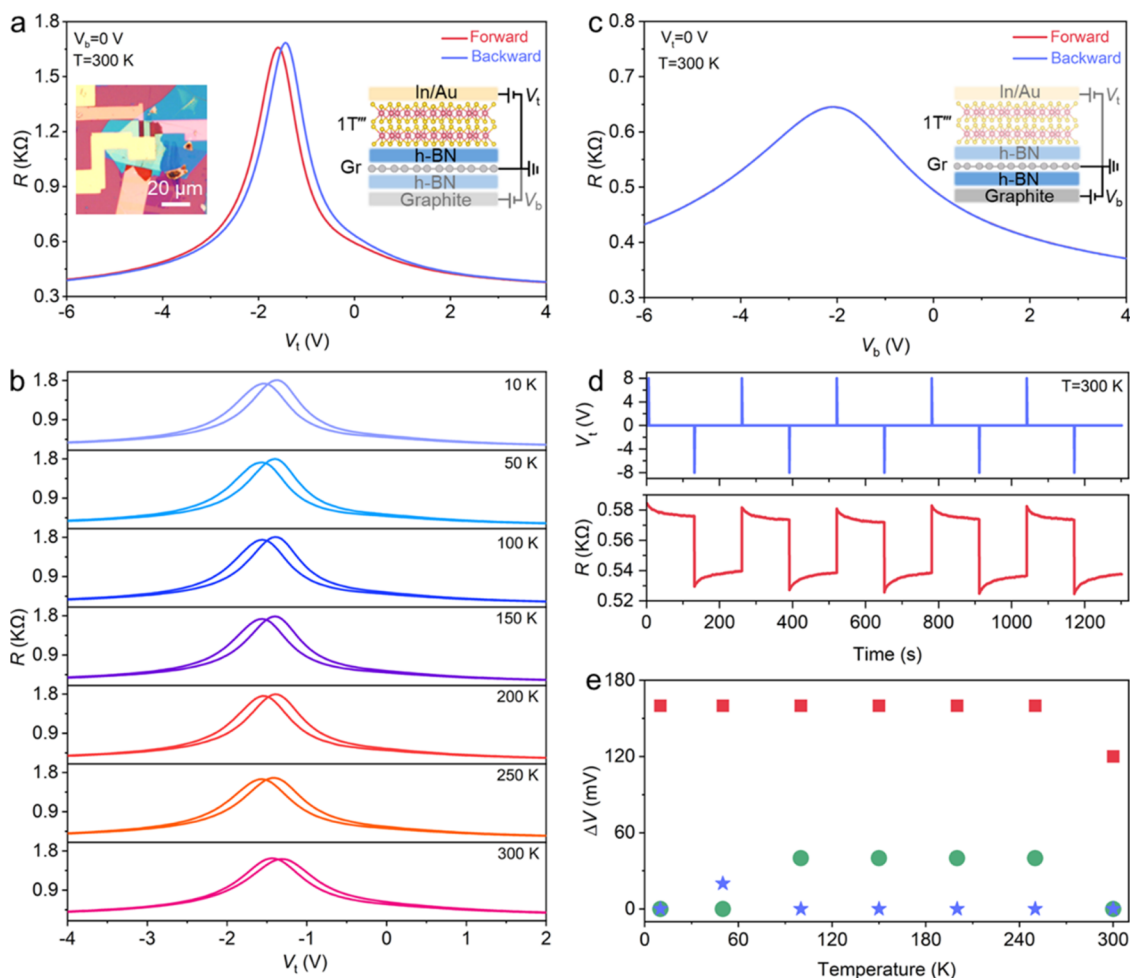
Figure 5. Probing the out-of-plane polarization of 1T′′′-MoS$_2$ by using graphene as the sensor. (a) Resistance of graphene in the FET device with a single-layered graphene as a channel using 1T′′′-MoS$_2$ as gate dielectrics as a function of V_t in the forward (red) and backward (blue) scan directions with V_b = 0 V and T = 300 K. Insets, the optical image and the cross-sectional schematic for the device used to apply an electric field perpendicular to both the 1T′′′-MoS$_2$ and graphene. (b) Resistance of graphene as a function of V_t in the forward and backward scan directions with V_b = 0 V at temperatures from 10 to 300 K. (c) Resistance of graphene as a function of V_b in the forward and backward scan directions with V_t = 0 V and T = 300 K, where the red line overlaps with the blue line. Inset, the cross-sectional schematic showing the application of bottom gate voltage. (d) Reversible switching of the resistance of graphene after V_t = ±8 V was applied to polarize 1T′′′-MoS$_2$ at T = 300 K over multiple circles. (e) Shift of gate voltages (ΔV) corresponding to the graphene resistance peak as a function of temperature. The red square, aqua circle, and azury star were derived from the data of the graphene resistance in FET devices as functions of V_t with 1T′′′-MoS$_2$ at V_b = 0 V (b), V_b with graphite at V_t = 0 V (Figure S18b), and V_t with 2H-MoS$_2$ at V_b = 0 V (Figure S20c), respectively. The graphene in the above devices was measured at a bias voltage of 10 mV.

graphene and the electric field across the 1T′′′-MoS$_2$. The bottom gate primarily changes the former, while the top gate alters both.[22] We first recorded the resistance of monolayer graphene as a function of V_t in the forward (red) and backward (blue) scan directions when V_b was set to 0 V at 300 K (Figure 5a). The gate voltages corresponding to the maximum resistance of the monolayer graphene shifted by ∼120 mV (ΔV) as the scanning direction changed. In addition, the abrupt split features of resistance were observed at V_t = −7.6 V and V_t = +7.2 V due to ferroelectric switching[22] (Figure S19). The hysteresis of the graphene transistor with 1T′′′-MoS$_2$ gating strengthened at low temperatures (Figure 5b,e). In contrast, no hysteresis (ΔV ∼ 0 mV) was observed during V_b scanning at a fixed V_t (Figure 5c), and it remained invariable at low temperatures (Figures 5e and S18b). This comparison result indicates that the ferroelectricity of the top gate 1T′′′-MoS$_2$ causes a shift in the gate voltage position corresponding to the peak resistance of graphene. Reversible ferroelectric

polarization switching was also tested with repeated polling at V_t of ±8 V (Figures 5d and S18c). For comparison, the same device was annealed at 260 °C and subsequent measurements did not observe any top gate hysteresis at varied temperatures (Figures 5e and S20), excluding the possible hysteresis arising from the interface or defect charge trapping.

CONCLUSIONS

In summary, we have successfully demonstrated the existence of room-temperature out-of-plane ferroelectricity in 2D metastable 1T′′′-MoS$_2$, with a Curie temperature of ∼350 K. Using a controlled two-step reduction−oxidation process via utilizing a single precursor, 2D high-purity 1T′′′-MoS$_2$ with a noncentrosymmetric $\sqrt{3}a \times \sqrt{3}a$ superlattice structure was acquired as evidenced by STEM, LFM, and SHG measurements. The ferroelectric property of 2D 1T′′′-MoS$_2$ was proved by creating ferroelectric domains by an electric field based on PFM and its electric polarization states could be detected and

switched by two types of FET devices. DFT calculations indicated that the out-of-plane spontaneous polarization of 1T‴-MoS$_2$ inherently arises from the intralayer charge transfer of S atoms. Our work illustrates that intrinsic ferroelectricity can be present in 2D 1T‴-MoS$_2$, adding more functionality to the 2D MoS$_2$ family. Furthermore, by controlling the stacking of 2D MoS$_2$ with varying phases and properties, it is highly feasible to create multifunctional ultrathin devices composed entirely of 2D MoS$_2$.

EXPERIMENTAL SECTION

Preparation of 2D 1T‴-MoS$_2$. The precursor K$_2$MoS$_4$ was prepared following previously reported procedures.[17] 300 mg K$_2$MoS$_4$ powders were placed in the center of a tube furnace under atmospheric pressure. The furnace was then heated to 770 °C with an Ar flow rate of 100 sccm (standard cubic centimeter per minute) and maintained at the temperature for 1 h. The reductive mixture gas of 20 sccm H$_2$ and 80 sccm Ar was then introduced to produce K$_x$MoS$_2$ crystals and maintained for 6 h at 770 °C. Afterward, the furnace was allowed to cool naturally to room temperature. The products were thoroughly rinsed with distilled water before being treated with an aqueous solution of K$_2$Cr$_2$O$_7$ (0.02 M) in sulfuric acid (0.1 M) using a mass ratio of K$_x$MoS$_2$/K$_2$Cr$_2$O$_7$ = 1:5. The obtained products were then washed with distilled water several times. After being dried in a vacuum freeze-dryer, 1T‴-MoS$_2$ crystals with high purity were finally obtained. The 2H-MoS$_2$ crystals were obtained by annealing 1T‴-MoS$_2$ crystals in Ar at 260 °C for 2 h. The 2D MoS$_2$ flakes with varied phases were mechanically exfoliated by tape for further characterization and device fabrication. For the PFM measurement, 2D 1T‴-MoS$_2$ flakes were obtained by gold-assisted mechanical exfoliation with electron beam evaporation (Figure S9).

Microscopic and Spectroscopic Characterizations. Optical images were taken with a BX 51 M microscope (Olympus). Raman spectroscopy measurements were conducted with a Raman system (HORIBA–Jobin–Yvon) at a 532 nm laser with a power of 1 mW. XRD patterns were identified with a D8 Advance (Bruker) instrument with Cu Kα radiation at 40 kV and 40 mA. SEM and EDS mapping images were collected with a Gemini 500 instrument (Zeiss). XPS spectra were measured with an ESCALAB 250Xi+ instrument (Thermo Fisher Scientific). AFM and lattice images were captured with a Dimension Icon instrument (Bruker) in tapping mode and a Cypher VRS (Oxford) in lateral force microscope mode, respectively. STEM images were obtained with a Spectra 300 (Thermo Fisher Scientific) at 200 kV.

SHG Measurements. Optical SHG signals were performed using Stanford SR830 DSP lock-in amplifiers equipped with a light conversion PHAROS femtosecond laser and heating accessories (Linkam HFS600E-PB4). The ultrafast pulse light of ~900 nm was used as the excitation source. The laser was focused using 20× objective lenses, producing a spot with a diameter of around 5.5 μm. With the polarization light held constant, the sample was rotated with steps of 3° to measure the spectra at different angles.

PFM Measurements. The ferroelectric polarizations of 2D 1T‴-MoS$_2$ flakes were conducted by a PFM (Bruker Dimension Icon) at room temperature in resonance-enhanced mode with conductive Pt/Ir tips of 3 N·m^{-1}. The resonance frequencies for the out-of-plane measurement were set at 300 kHz. The PFM hysteresis loops were measured by applying a tip bias of ±10 V to the samples.

Device Fabrication and Measurements. Two layouts of FET devices with 1T‴-MoS$_2$ were prepared: (1) a 1T‴-MoS$_2$ flake served as the channel, connected to source and drain electrodes, and was encapsulated between two h-BN flakes using single-layered graphene and graphite as the top and bottom gate electrodes, respectively (Figure 4a) and (2) a single-layered graphene served as the channel, connected to source and drain electrodes, and was encapsulated between two h-BN using 1T‴-MoS$_2$ as top gate dielectrics and graphite as bottom gate electrodes, respectively (Figure 5a). Next, we described the fabrication process for the first type of device; the

process for preparing the second type of device was similar. First, graphite flakes were exfoliated onto SiO$_2$ (300 nm)/Si substrates as bottom gate electrodes, followed by annealing in a gas flow of 5 sccm H$_2$ and 95 sccm Ar at 350 °C for more than 2 h to remove the tape residues. Monolayer graphene, h-BN, and 1T‴-MoS$_2$ were exfoliated onto poly(dimethylsiloxane) (PDMS) and vertically stacked via the layer-by-layer dry transfer method (Figure S13). The h-BN, serving as the dielectric layer, was transferred over the graphite flake. The channel material of 1T‴-MoS$_2$ was then placed on the top of h-BN, and the In/Au (7 nm/15 nm) electrodes as the source and drain were patterned on 1T‴-MoS$_2$ by electron beam lithography (EBL), thermal evaporation, and lift-off. Subsequently, h-BN was stacked as the dielectric layer above the 1T‴-MoS$_2$, and then the monolayer graphene, serving as the top gate electrode, was transferred onto the h-BN. Finally, EBL and metallization were used to ensure proper electrical contacts of In/Au (10 nm/60 nm) with In/Au electrodes (8 nm/10 nm) and the top monolayer graphene and bottom graphite. The thickness of each layer in the two types of devices is listed in Table S1. All electrical transport measurements were performed in a cryogenic probe station equipped with a Keithley 4200A semiconductor analyzer under vacuum (10^{-5} mbar).

Theoretical Calculations. DFT calculations were performed using the Vienna *Ab initio* Simulation Package (VASP). The Perdew–Burke–Ernzerhof (PBE) functional was employed to describe the exchange–correlation interaction, along with the vdW correction to account for vdW interactions. The projector augmented wave (PAW) method was used to describe the electron–ion interaction between the core and valence electrons. We set an energy cutoff of 600 eV. Geometry optimizations were carried out using the conjugate gradient algorithm until the forces converged below 0.01 V·Å^{-1}. Charge self-consistent calculations were converged to 10^{-7} eV. The Brillouin zone was sampled using a 7 × 7 × 1 k-point Monkhorst–Pack mesh. The vacuum region of the structure model was set to be thicker than 15 Å. To correct the electrostatic interaction between dipole layers, a dipole correction was applied by introducing a planar dipole layer in the middle of the vacuum region, as performed in the VASP.

ASSOCIATED CONTENT

Ⓢ Supporting Information

The Supporting Information is available free of charge at https://pubs.acs.org/doi/10.1021/acsnano.4c03608.

Theoretical calculations of ferroelectric polarization in monolayer and bilayer 1T‴-MoS$_2$, layer-dependent band gaps (E_g) of 2D 1T‴-MoS$_2$ caused by the depolarization field, more SEM, EDS, and XPS measurements of K$_{0.3}$MoS$_2$, 1T‴-MoS$_2$, and 2H-MoS$_2$ crystals, lattice structures of 2D 1T′-MoS$_2$ and 2H-MoS$_2$ flakes imaged via LFM, SHG characterizations of 2D 1T‴-MoS$_2$ flakes, sample preparation for PFM measurements, fabrication process of the FET device with 1T‴-MoS$_2$ as a channel, electrical measurements of 1T‴-MoS$_2$ and the FET device with 1T‴-MoS$_2$ as a channel, phase transition of 1T‴-MoS$_2$ by thermal annealing, electrical measurements of the FET device with 1T‴-MoS$_2$ as gate dielectrics, thickness of graphite, graphene, h-BN dielectrics, and 1T‴-MoS$_2$ for FET devices of Figures 4a and 5a in the main text (PDF)

AUTHOR INFORMATION

Corresponding Authors

Yaming Zhou — *Key Laboratory of Organic Optoelectronics and Molecular Engineering of the Ministry of Education, Department of Chemistry, Tsinghua University, Beijing 100084, China*; Email: ymzhou@mail.tsinghua.edu.cn

Shi Liu — *Institute of Natural Sciences, Westlake Institute for Advanced Study, Hangzhou 310024 Zhejiang, China;*

Department of Physics, School of Science, Westlake
University, Hangzhou 310024 Zhejiang, China;
 orcid.org/0000-0002-8488-4848; Email: liushi@
westlake.edu.cn

Liming Xie − *CAS Key Laboratory of Standardization and
Measurement for Nanotechnology, National Center for
Nanoscience and Technology, Beijing 100190, China;
University of Chinese Academy of Sciences, Beijing 100049,
China;* orcid.org/0000-0001-8190-8325; Email: xielm@
nanoctr.cn

Liying Jiao − *Key Laboratory of Organic Optoelectronics and
Molecular Engineering of the Ministry of Education,
Department of Chemistry, Tsinghua University, Beijing
100084, China;* orcid.org/0000-0002-6576-906X;
Email: lyjiao@mail.tsinghua.edu.cn

Authors

Changan HuangFu − *Key Laboratory of Organic
Optoelectronics and Molecular Engineering of the Ministry of
Education, Department of Chemistry, Tsinghua University,
Beijing 100084, China*

Changming Ke − *Institute of Natural Sciences, Westlake
Institute for Advanced Study, Hangzhou 310024 Zhejiang,
China; Department of Physics, School of Science, Westlake
University, Hangzhou 310024 Zhejiang, China*

Junyi Liao − *Key Laboratory of Organic Optoelectronics and
Molecular Engineering of the Ministry of Education,
Department of Chemistry, Tsinghua University, Beijing
100084, China; CAS Key Laboratory of Standardization
and Measurement for Nanotechnology, National Center for
Nanoscience and Technology, Beijing 100190, China;
University of Chinese Academy of Sciences, Beijing 100049,
China*

Jiangcai Wang − *State Key Laboratory of Tribology in
Advanced Equipment, Tsinghua University, Beijing 100084,
China*

Huan Liu − *State Key Laboratory of Tribology in Advanced
Equipment, Tsinghua University, Beijing 100084, China*

Dameng Liu − *State Key Laboratory of Tribology in Advanced
Equipment, Tsinghua University, Beijing 100084, China;*
 orcid.org/0000-0003-1957-4250

Complete contact information is available at:
https://pubs.acs.org/10.1021/acsnano.4c03608

Notes
The authors declare no competing financial interest.

REFERENCES
(1) Khan, A. I.; Chatterjee, K.; Wang, B.; Drapcho, S.; You, L.;
Serrao, C.; Bakaul, S. R.; Ramesh, R.; Salahuddin, S. Negative
capacitance in a ferroelectric capacitor. *Nat. Mater.* **2015**, *14*, 182−
186.
(2) Íñiguez, J.; Zubko, P.; Luk'yanchuk, I.; Cano, A. Ferroelectric
negative capacitance. *Nat. Rev. Mater.* **2019**, *4*, 243−256.
(3) Liao, J.; Wen, W.; Wu, J.; Zhou, Y.; Hussain, S.; Hu, H.; Li, J.;
Liaqat, A.; Zhu, H.; Jiao, L.; et al. Van der Waals ferroelectric
semiconductor field effect transistor for in-memory computing. *ACS
Nano* **2023**, *17*, 6095−6102.
(4) Jin, T. Y.; Mao, J. Y.; Gao, J.; Han, C.; Wee, A. T. S.; Loh, K. P.;
Chen, W. Ferroelectrics-integrated two-dimensional devices toward
next-generation electronics. *ACS Nano* **2022**, *16*, 13595−13611.
(5) Si, M.; Liao, P. Y.; Qiu, G.; Duan, Y.; Ye, P. D. Ferroelectric
field-effect transistors based on MoS₂ and CuInP₂S₆ two-dimensional
van der Waals heterostructure. *ACS Nano* **2018**, *12*, 6700−6705.
(6) Si, M.; Zhang, Z.; Chang, S. C.; Haratipour, N.; Zheng, D.; Li, J.;
Avci, U. E.; Ye, P. D. Asymmetric metal/α-In₂Se₃/Si crossbar
ferroelectric semiconductor junction. *ACS Nano* **2021**, *15*, 5689−
5695.
(7) Fei, Z.; Zhao, W.; Palomaki, T. A.; Sun, B.; Miller, M. K.; Zhao,
Z.; Yan, J.; Xu, X.; Cobden, D. H. Ferroelectric switching of a two-
dimensional metal. *Nature* **2018**, *560*, 336−339.
(8) Yuan, S.; Luo, X.; Chan, H. L.; Xiao, C.; Dai, Y.; Xie, M.; Hao, J.
Room-temperature ferroelectricity in MoTe₂ down to the atomic
monolayer limit. *Nat. Commun.* **2019**, *10*, No. 1775.
(9) Ghosh, T.; Samanta, M.; Vasdev, A.; Dolui, K.; Ghatak, J.; Das,
T.; Sheet, G.; Biswas, K. Ultrathin free-standing nanosheets of
Bi₂O₂Se: room temperature ferroelectricity in self-assembled charged
layered heterostructure. *Nano Lett.* **2019**, *19*, 5703−5709.
(10) Lipatov, A.; Chaudhary, P.; Guan, Z.; Lu, H.; Li, G.; Crégut,
O.; Dorkenoo, K. D.; Proksch, R.; Cherifi-Hertel, S.; Shao, D.-F.; et al.
Direct observation of ferroelectricity in two-dimensional MoS₂. *npj
2D Mater. Appl.* **2022**, *6*, No. 18, DOI: 10.1038/s41699-022-00298-5.
(11) Wypych, F.; Weber, T.; Prins, R. Scanning tunneling
microscopic investigation of 1T-MoS₂. *Chem. Mater.* **1998**, *10*,
723−727.
(12) Shirodkar, S. N.; Waghmare, U. V. Emergence of ferroelec-
tricity at a metal-semiconductor transition in a 1T monolayer of
MoS₂. *Phys. Rev. Lett.* **2014**, *112*, No. 157601.
(13) Bruyer, E.; Di Sante, D.; Barone, P.; Stroppa, A.; Whangbo, M.
H.; Picozzi, S. Possibility of combining ferroelectricity and Rashba-
like spin splitting in monolayers of the 1T-type transition-metal
dichalcogenides MX₂ (M = Mo, W; X = S, Se, Te). *Phys. Rev. B* **2016**,
94, No. 195402.
(14) Zhuang, H. L.; Johannes, M. D.; Singh, A. K.; Hennig, R. G.
Doping-controlled phase transitions in single-layer MoS₂. *Phys. Rev. B*
2017, *96*, No. 165305.
(15) Lai, Z.; He, Q.; Tran, T. H.; Repaka, D. V. M.; Zhou, D. D.;
Sun, Y.; Xi, S.; Li, Y.; Chaturvedi, A.; Tan, C.; et al. Metastable 1T′-
phase group VIB transition metal dichalcogenide crystals. *Nat. Mater.*
2021, *20*, 1113−1120.
(16) Fang, Y. Q.; Hu, X. Z.; Zhao, W.; Pan, J.; Wang, D.; Bu, K. J.;
Mao, Y. L.; Chu, S. F.; Liu, P.; Zhai, T. Y.; Huang, F. Structural
determination and nonlinear optical properties of new 1T‴-Type
MoS₂ compound. *J. Am. Chem. Soc.* **2019**, *141*, 790−793.
(17) Liu, L.; Wu, J.; Wu, L.; Ye, M.; Liu, X.; Wang, Q.; Hou, S.; Lu,
P.; Sun, L.; Zheng, J.; et al. Phase-selective synthesis of 1T′ MoS₂
monolayers and heterophase bilayers. *Nat. Mater.* **2018**, *17*, 1108−
1114.
(18) Vasudevan, R. K.; Balke, N.; Maksymovych, P.; Jesse, S.;
Kalinin, S. V. Ferroelectric or non-ferroelectric: why so many
materials exhibit "ferroelectricity" on the nanoscale. *Appl. Phys. Rev.*
2017, *4*, No. 021302.
(19) Malard, L. M.; Alencar, T. V.; Barboza, A. P. M.; Mak, K. F.; de
Paula, A. M. Observation of intense second harmonic generation from
MoS₂ atomic crystals. *Phys. Rev. B* **2013**, *87*, No. 201401(R).
(20) Si, M.; Saha, A. K.; Liao, P. Y.; Gao, S.; Neumayer, S. M.; Jian,
J.; Qin, J.; Balke Wisinger, N.; Wang, H.; Maksymovych, P.; et al.
Room-temperature electrocaloric effect in layered ferroelectric

CuInP$_2$S$_6$ for solid-state refrigeration. *ACS Nano* **2019**, *13*, 8760−8765.

(21) Sharma, P.; Xiang, F. X.; Shao, D. F.; Zhang, D.; Tsymbal, E. Y.; Hamilton, A. R.; Seidel, J. A room-temperature ferroelectric semimetal. *Sci. Adv.* **2019**, *5*, No. eaax5080.

(22) Wang, X.; Yasuda, K.; Zhang, Y.; Liu, S.; Watanabe, K.; Taniguchi, T.; Hone, J.; Fu, L.; Jarillo-Herrero, P. Interfacial ferroelectricity in rhombohedral-stacked bilayer transition metal dichalcogenides. *Nat. Nanotechnol.* **2022**, *17*, 367−371.